

Interacting single atoms with nanophotonics for chip-integrated quantum networks

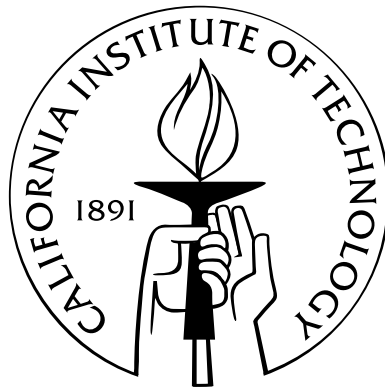
Thesis by

Daniel James Alton

In Partial Fulfillment of the Requirements

for the Degree of

Doctor of Philosophy



California Institute of Technology

Pasadena, California

2013

(Defended May 22, 2013)

© 2013

Daniel James Alton

All Rights Reserved

To my parents, sister, and loved ones.

Acknowledgments

First and foremost, I would like to thank God, the Almighty, for all of His blessings.

I would like to thank my advisor, professor Jeff Kimble, a mentor who I greatly respect and admire. Not just as a great scientist with exceptionally high standards of rigor and integrity, but it never cease to amaze me, professor Kimble's depth and breadth of thinking. Looking into matters from the biggest horizon to the smallest details, connecting the many dots and people to the matter, and looking far into the future and down to the shortest time scales in the experiment. It has been a great privilege and I am deeply grateful.

I would like to thank our collaborators, professor Kerry Vahala and professor Oskar Painter, for sharing their pioneering expertise and leadership in the development of novel photonic devices, with very high, world-record quality, which have been critical in the work described in this thesis. My thesis committee members, professor Jeff Kimble, professor Kerry Vahala, professor Olexei Motrunich, and professor Michael Roukes, who have been extraordinary sources of inspirations, thank you very much.

My sincere gratitude to professor Peter Zoller and professor Jun Ye, visiting professors in our group who have shared their insights and advice for certain parts of the work described in this thesis. To professor Jun Ye, for inviting me to spend a week at his laboratory at JILA, Boulder, Colorado, to learn about the making of optical amplifiers, and to the members in the Ye group, especially Sebastian Blatt.

The work described in this thesis is a result of contributions and hard work of many individuals that I would like to acknowledge here. In the experiments with microtoroidal resonators: Takao Aoki, a very talented scientist and experimentalist that I admire and learn greatly from; Scott Parkins, who enlightened us with the fundamental theoretical formulations especially in our photon router work; Nate Stern, a multi-talented scientist whose work and drive I admire both in the experimental and theoretical parts of our work; Hansuek Lee and Eric Ostby from Vahala group, highly talented individuals who shared their expertise and fabricated the wonderful microtoroidal photonic devices

critical in our experiments; last but not least, Cindy Regal and Barak Dayan, extraordinary scientists whose works are simply amazing. In the experiments with optical nanofibers: Kyung Soo Choi and Akihisa Goban, extraordinarily talented and accomplished young scientists who I especially commend and thankful to not just for our collaboration in the lab but also outside of the lab for our enduring friendship. Ding Ding, Clement Lacroute, Martin Pototschnig, and Tobias Thiele, who made important contributions in our nanofiber trap work. In the experiments with photonic crystal based structures: Firstly in Lab 11, Akihisa Goban and Chen-Lung Hung whose cold atom transport design formed the basis of the experimental setup in Lab 1 discussed in this thesis. Chen-Lung's extraordinary talent and exceptionally open-minded approach had been critical and greatly valuable in the projects; The photonic crystal based device design/characterization/fabrication team: Su-Peng Yu, Jonathan Hood (Kimble group), Richard Norte, Sean Meneehan, and Justin Cohen (Painter group), whose work have been critical in our experiments; In Lab 2: Jae Hoon Lee, Juan Muniz, and Ding Ding; Thanks especially to Juan Muniz for our close collaboration in investigating atom trapping schemes, where Juan's great talents and contributions have been critical; Last but not least, the team in Lab 1 who have directly worked in the photonic crystal based experiments discussed in this thesis: Andrew McClung, an exceptionally talented researcher and computer expert whose combination with out-of-the-box thinking have led to various major contributions in our lab; Pol Forn-Diaz, a very talented scientist with broad interests and at the same time extraordinary attention to details, who I greatly respect and am thankful for to have worked together inside and outside of the lab; Martin Pototschnig, an insightful and highly talented experimentalist, who is capable of achieving amazing results especially when the insights are unleashed; and Clement Lacroute, for his important and valuable contributions. I also want to acknowledge Taofiq Paraiso and Alex Krause from Painter group.

I would like to thank the members of the Kimble group (Caltech Quantum Optics group), Vahala and Painter groups, and the Institute for Quantum Information and Matter (IQIM) at Caltech, who have been great sources of inspirations, friendships and supports at various locations, times, and situations, I am greatly thankful for these years where our paths have crossed, and hopeful that they will again in the future. In addition to the above-mentioned, I would like to specifically thank: Dalziel Wilson, Yi Zhao, Kang-Kuen Ni, Scott Papp, Russ Miller, Hui Deng, Tracy Northup, Julien Laurat, Elizabeth Wilcut Connolly, Scott Kelber, Daniel Chao, Sarah Kaiser, Michael Martin, Jiang Li, Kiyoul Yang, Darrick Chang, Alexey Gorshkov, Liang Jiang, K C Fong, and Matt Eichenfield. I would like to thank Scott Curtis our group's administrator who always got the job done exceptionally

well regardless of the number of lines, people, organizations, or challenges involved. I also want to thank several particular administrators in the Physics department, Donna Driscoll, Marcia Brown, Alan Rice, Louisa Fung, and Loly Ekmekjian.

I would like to take this opportunity to thank my undergraduate research advisors, Prof. Ping Koy Lam, Prof. Tim Ralph, and Dr. Thomas Symul, at Australian National University and University of Queensland, who have introduced me to the world of quantum optics, to whom I am greatly and always be thankful.

I would like to thank my parents, sister, and grandparents, who have given their endless support, inspirations, and love in my life. I am forever grateful for their sacrifices, guidance and faith in me. Despite the extend of the oceans, masses of land, and the four different time zones that I have lived in for extended periods of time, they have always been there. I am blessed to have met a very special person whom I hold close and dear, who has enriched my life in every aspect since the last two years. I thank her for all the love and support. It is to them, I wish to dedicate this thesis.

Daniel Alton
May 2013
Pasadena, CA

Abstract

Underlying matter and light are their building blocks of tiny atoms and photons. The ability to control and utilize matter-light interactions down to the elementary single atom and photon level at the nano-scale opens up exciting studies at the frontiers of science with applications in medicine, energy, and information technology. Of these, an intriguing front is the development of quantum networks where $N \gg 1$ single-atom nodes are coherently linked by single photons, forming a collective quantum entity potentially capable of performing quantum computations and simulations. Here, a promising approach is to use optical cavities within the setting of cavity quantum electrodynamics (QED). However, since its first realization in 1992 by Kimble et al., current proof-of-principle experiments have involved just one or two conventional cavities. To move beyond to $N \gg 1$ nodes, in this thesis we investigate a platform born from the marriage of cavity QED and nanophotonics, where single atoms at ~ 100 nm near the surfaces of lithographically fabricated dielectric photonic devices can strongly interact with single photons, on a chip. Particularly, we experimentally investigate three main types of devices: microtoroidal optical cavities, optical nanofibers, and nanophotonic crystal based structures. With a microtoroidal cavity, we realized a robust and efficient photon router where single photons are extracted from an incident coherent state of light and redirected to a separate output with high efficiency. We achieved strong single atom-photon coupling with atoms located ~ 100 nm near the surface of a microtoroid, which revealed important aspects in the atom dynamics and QED of these systems including atom-surface interaction effects. We present a method to achieve state-insensitive atom trapping near optical nanofibers, critical in nanophotonic systems where electromagnetic fields are tightly confined. We developed a system that fabricates high quality nanofibers with high controllability, with which we experimentally demonstrate a state-insensitive atom trap. We present initial investigations on nanophotonic crystal based structures as a platform for strong atom-photon interactions. The experimental advances and theoretical investigations carried out in this thesis provide a framework for and open the door to strong single atom-photon interactions using nanophotonics for chip-integrated quantum networks.

Contents

Acknowledgments	iv
Abstract	vii
1 Introduction	1
1.1 Context and motivation	1
1.1.1 Optics and photonics: past and present	1
1.1.2 Nanophotonic single atom-photon interaction and the future	4
1.1.2.1 Medicine	5
1.1.2.2 Energy	6
1.1.2.3 Information technology	7
1.1.3 The quantum internet	8
1.1.3.1 Quantum metrology	9
1.1.3.2 Quantum cryptography	9
1.1.3.3 Quantum computer	11
1.1.3.4 The marriage of cavity QED and nanophotonics	14
1.2 Thesis outline	15
2 Atom-photon interactions	18
2.1 Introduction	18
2.2 One atom and a single photonic mode	20
2.3 Interaction in the weak coupling regime ($g \ll \kappa, \Gamma_0$)	22
2.4 Interaction in the strong coupling regime ($g \gg \kappa, \Gamma_0$)	24
2.4.1 Optical cavity	25
2.4.2 Cavity QED	26
2.5 Platforms for atom-photon interactions	30

2.5.1	Atom-photon interactions without a cavity	31
2.5.1.1	Free-space	31
2.5.1.2	Nanophotonic waveguides	33
2.5.2	Atom-photon interactions within a cavity	37
2.5.2.1	Fabry-Perot cavity	39
2.5.2.2	Microtoroidal cavity	39
2.5.2.3	Nanophotonic cavities	42
3	Experimental overview	46
3.1	Cavity QED with a microtoroidal cavity	47
3.1.1	Model	47
3.1.1.1	Modes of a microtoroidal resonator	47
3.1.1.2	Fiber-toroid optical coupling	49
3.1.1.3	Cavity QED in an axisymmetric resonator	55
3.1.2	Experiment setup and techniques	59
3.1.2.1	Cold atoms and conveyor belt	61
3.1.2.2	Optics and electronics	65
3.1.2.3	Optical/photonic devices and mechanics	67
3.2	Nanophotonic optical fiber as a quantum optics platform	69
3.2.1	Model	69
3.2.1.1	Fundamental nanofiber mode	71
3.2.1.2	Atom-photon interactions with nanofibers	75
3.2.2	Experiment and fabrication setups	78
3.3	Nanophotonic waveguide and cavity as a cavity QED platform	79
3.3.1	Single nanobeam	81
3.3.2	Double nanobeam	84
3.3.3	Experiment setup and techniques	86
3.4	Summary	91
4	Efficient routing of single photons by one atom and a microtoroidal cavity	93
4.1	Introduction	93
4.2	Background	94
4.3	Model	95

4.4	Theoretical results	97
4.5	Experimental setup	97
4.6	Experimental results	99
4.7	Summary	102
5	Strong interactions of single atoms and photons near a dielectric boundary	103
5.1	Introduction	103
5.2	Background	104
5.3	Real time single atom detection	107
5.4	Experimental results	108
5.5	Atom trajectories near a microtoroid	110
5.6	Spectral measurements	110
5.7	Photon statistics	115
5.8	Detailed microtoroid cQED theory	115
5.9	Experiment scheme and setup	118
5.9.1	Real time detection of atom transits	121
5.10	Modeling ensembles of atoms detected in real time	123
5.10.1	Analytic model for real time detection distributions	123
5.10.2	Full Monte Carlo simulation	124
5.10.2.1	Dipole force	124
5.10.2.2	Spontaneous emission rate near a surface	125
5.10.2.3	Casimir-Polder interactions	125
5.11	Additional cQED spectra	126
5.12	Summary	127
6	Dynamics and trapping of atoms near dielectric surfaces	129
6.1	Introduction	129
6.2	Simulations of atomic trajectories near a dielectric surface	130
6.2.1	Background	130
6.2.2	Atoms in a microtoroidal cavity	132
6.2.2.1	Modes of a microtoroidal resonator	133
6.2.2.2	Cavity QED in an axisymmetric resonator	133
6.2.3	Optical forces on an atom in a cavity	133

6.2.3.1	Dipole forces	133
6.2.3.2	Velocity-dependent forces on an atom	134
6.2.3.3	Momentum diffusion and the diffusion tensor in a cavity	135
6.2.4	Effects of surfaces on atoms near dielectrics	135
6.2.4.1	Spontaneous emission rate near a surface	136
6.2.4.2	Calculation of Casimir-Polder potentials	136
6.2.5	Simulating atoms detected in real-time near microtoroids	139
6.2.5.1	Simulation procedure	141
6.2.5.2	Simulation distributions	143
6.2.5.3	Simulated trajectories	145
6.2.6	Calculating the polarizability and dielectric response functions	148
6.2.7	Analytic model of falling atom detection distributions	149
6.3	Trapping of atoms near dielectric surfaces	151
6.3.1	Optical tweezer trap	152
6.3.2	Orbiting trap	153
6.3.2.1	Trapping atoms in the evanescent field of a microtoroid	153
6.3.2.2	Microtoroidal cavity modes, spectrum and tunability	156
6.3.3	Toroid-fiber trap	159
7	A state-insensitive, compensated nanofiber trap	166
7.1	Background	167
7.2	Scheme and trap potential	167
7.2.1	Introduction	167
7.2.2	Scheme	169
7.2.3	Light shift Hamiltonian	172
7.2.4	Cancellation of the vector shifts	174
7.2.5	Magic wavelengths for an evanescent field trap	175
7.2.6	Trap potential and compensation comparison	176
7.2.6.1	Trap potential without compensation scheme	177
7.2.6.2	Trap potential with compensation scheme	179
7.2.6.3	Trap potential of nanofiber trap experiment	181
7.3	Fabrication of a tapered nanofiber	181
7.3.1	Nanofiber fabrication setup	184

7.3.2	Trajectories of pulling motors	187
7.3.3	Nanofiber profile	188
7.3.4	Adiabaticity and transmission efficiency	191
7.3.5	Optical power handling	195
7.4	Nanofiber trap experiment	196
7.5	Summary	199
8	Investigations of nanophotonic waveguides and cavities for strong atom-photon interactions	202
8.1	Introduction	202
8.2	Platform	204
8.2.1	Nanobeam waveguides	204
8.2.2	Cold atoms	207
8.2.3	Cavity QED with nanobeams	210
8.2.3.1	Cavity temperature tuning	211
8.2.4	Experimental setup	214
8.3	Atom trapping schemes	219
8.3.1	Atom trapping with a single nanobeam	219
8.3.1.1	Magic-compensated scheme with wavelength contrast	220
8.3.1.2	Small detuning with orthogonal polarizations	221
8.3.1.3	External illumination with an auxiliary nanobeam	223
8.3.1.4	External illumination without phase coherence	225
8.3.1.5	External illumination with phase coherence	227
8.3.1.6	Hybrid external illumination and guided mode excitation	228
8.3.2	Atom trapping with a double nanobeam	230
8.3.2.1	External illumination with an auxiliary nanobeam	230
8.3.2.2	Corrugated double nanobeam	230
8.3.2.3	Guided mode with a blue trap	232
8.3.2.4	Two-color trap with RF switching	235
A	Attocube positioner characterization	239
	Bibliography	244

List of Figures

- 1.1 **Top:** Optics and photonics applications in medicine, information technology and energy, sorted by the number of photons along the radial axis, for radio/microwave (labelled in green), visible/infrared (black), and x-ray (red) photons. The number labels are ordered in increasing optical power, which correspond to Table 1.1. **Center:** Single atom and photon as the building block for elementary quantum matter-light interactions gives insights into future nanophotonics applications and powerful quantum technologies beyond the classical realm (bottom section), as predicted by celebrated physicist and Nobel laureate Richard Feynman in 1959. 2
- 2.1 **Overview of atom-photon interaction.** **a)** Two level atom interacting with a single photonic mode a_p at rate g . **b)** Dressed atom energy levels E_{jn} where $j = g, e$ for ground, excited states (dashed lines: absent atom-photon coupling). **c)** Excited atom decay rate into the photonic mode a_p (e.g., waveguide mode, intracavity mode), Γ_p , and decay (loss) rate to the environment, Γ_0 . The coupling rate between the mode a_p and detector is κ , which is equal to Γ_p in direct detection, but may be different than Γ_p for a cavity system. **d)** Probability P_e of an initially excited atom to be in the excited state after a time $g_{iv}t$ where $g_{iv} = 105\text{MHz}$. (i) Atom free-space decay rate $\Gamma_0/2\pi = 5.2\text{ MHz}$. (ii) Enhanced decay rate $\Gamma_p = 2\Gamma_0$. (iii) With $g/2\pi = 105\text{ MHz}$, $\kappa/2\pi = 20\text{ MHz}$, $\Gamma_0/2\pi = 5.2\text{ MHz}$ (Cesium D2 line) [5]. **e)** Atom-photon interaction strengths parametrized by $\chi = \Gamma_p/\Gamma_0$ for waveguides 1. to 3. and cavities 4. to 8. Limits are discussed in main text. Inset: Some data points showing χ realized in various experiments, 1a-1b: Nanofiber trap in [248] and [91], also with the corresponding cooperativity parameter C for cavity QED systems with Fabry-Perot (5a) [33], Microtoroid (7a-7b) [9] and [5]. 19

2.2 **Atom-photon interaction without a cavity. a,c,e,f)** Atom interacting with photonic mode a_p , $E(\omega_p)$ is the oscillating electric field at optical frequency ω_p ; σ^- and d_{ge} are atomic lowering operator and electric dipole moment; H_{int} : atom-photon interaction Hamiltonian; P_{in}, P_R, P_T : input, reflected, transmitted optical power; Γ_p and Γ_0 are decay rate into photonic mode a_p and decay (loss) rate into the environment respectively; A_{eff} and σ are photonic effective area and atomic scattering cross-section respectively. **c)** f : focal length of the pair of lenses; w_{in} : input Gaussian beam waist (radius) size. **b)** Cesium D2 line energy levels/manifolds. **d,g,h)** T, R : transmittance and reflectance; $R_{\text{Sc}} = \sigma_0/A_{\text{eff}}$, atom scattering rate, where σ_0 is the atomic resonant scattering cross-section. **d)** Results for strongly focused light; χ : full model; χ' : paraxial approximation; $u = w_{\text{in}}/f$, focusing strength; (i): Experimental result for T of [233]. **Top g)** Comparison between our approximate model (solid curves) and full results of [126] (dashed curves). **Bottom g)** Results using our model for parameters in [248] (fiber radius 250 nm) and [91] (fiber radius 215 nm) with measurements of $(1 - T)$ shown by (i) and (ii) respectively. The variable d is the atom to fiber's surface distance. **h)** Contour plot of χ . Points (i) and (ii) correspond to parameters in [248] and [91] respectively. **g,h)** As evident in g), the prediction model agrees with [91], point (ii), but this is not the case for [248], point (i). This is discussed further in the text.

2.3 Atom-photon interaction within a cavity. a,b,c,d) Q : cavity quality factor, V_m : cavity mode volume; P_{in}, P_R, P_T : input, reflected, transmitted optical powers; g : atom-photon coupling rate; κ_i : intrinsic cavity loss; κ_{ex} : extrinsic input/output coupling rate; E_{max} and $E(\vec{r}_a)$ are the maximum electric field and the electric field at atom's position \vec{r}_a ; Γ_p : atom's decay rate into cavity photonic mode; Γ_0 : atom's decay rate into the environment. **e,f)** C : cooperativity parameter; $\chi = \Gamma_p/\Gamma_0$; d = atom-to-surface distance. **a)** Fabry-Perot cavity; labels in e) and f): a1, experimental parameters of [33], a2, ultimate limit [33]. **b)** Microtoroidal cavity; labels in e) and f): b1 and b2, experimental parameters of [9] and [5], b3 and b4, projected limits [224, 131]. **c)** Atomic mirror cavity (formed by 2 N_m atoms): c1, prediction from [41] with $|E|/|E_{max}| = 0.33$, c2, with $|E|/|E_{max}| = 1$. **d)** Photonic crystal cavity: d1-d4 for currently realizable Q/V_m value to the projected limit [147], with $|E|/|E_{max}| = 0.5$, d5-d8 for same range of Q/V_m but with $|E|/|E_{max}| = 1$ and an enhancement factor of 10 in atom's decay rate into the photonic mode that may be gained by utilization of photonic crystal band structure effect. Note: a1, a2, d5-d8 indicate values of χ (with $\Gamma_0 = \gamma_0$, the free-space decay rate), they are not functions of d . The horizontal lines serve as visual guides for comparison with other curves. 45

3.1 Microtoroid cavity QED schematic. (a) Optical input/output coupling enabled by a tapered fiber (diameter D_f) positioned at a small fiber/toroid surface-to-surface gap $x_{ft} < \lambda$. Spatial cylindrical coordinates $\{\rho, \phi, z\}$ with origin at toroid center. The toroid geometry can be described by its major (D_M), minor (D_m), and principal (D_p) diameters. On the toroid's cross-sectional minor circle plane, ψ describes the latitudinal angle, and $d = d(\rho, z)$ is the atom-to-surface distance. **(b)** Tapered fiber optical input/output fields $\{a_{in}, a_{out}, b_{in}, b_{out}\}$ coupled at rate κ_{ex} to toroid counter-propagating intracavity fields $\{a, b\}$, coupled by internal scatterers at a rate h , suffering intrinsic loss at rate κ_i . A nearby atom located at \vec{r} is coupled to the cavity at rate $g(\vec{r})$, and has a free space spontaneous emission rate γ . **(c)** i-iv): normalized electric field $|E|$ profiles and the components $\{E_z^\theta, E_\rho^\theta, E_\phi^\theta\}$ (where θ indicates the optical phase), with $E_z^{max} = 1.00|E|^{max}$, $E_\rho^{max} = 0.086|E|^{max}$, $E_\phi^{max} = 0.118|E|^{max}$; v-vii) shows the lowest-order mode function $f(\rho, z)$ for a toroid with $\{D_p, D_m\} = \{24, 3\} \mu\text{m}$, $m = 118$ and $\lambda = 852 \text{ nm}$, and the cross-sections along d and z . **(d)** SEM images of two fabricated microtoroids with $D_p \sim 18 \mu\text{m}$ and $D_p \sim 24 \mu\text{m}$ 48

- 3.2 **Microtoroid-nanofiber optical coupling.** **a)** Nanofiber (radius a) and microtoroidal cavity (principal radius r_p , minor radius $r_m = 1.5 \mu\text{m}$) interacting over an effective interaction length L_{ft} , with gap x_{ft} , modeled as two parallel cylindrical waveguides. **b)** Transverse cross-section of a pair of generic waveguides (a, b), with electric fields (E_a, E_b) , individual (one waveguide) refractive index profiles (n_a, n_b) , and composite (two waveguides) refractive index profile n_c , along a spatial coordinate r . **c)** Dispersion curves near phase-matching frequency ω_0 ; β_a, β_b : no coupling; γ_1, γ_2 : lowest order odd and even supermodes; δ : phase-matching coefficient. **d)** Fiber V -parameter, $V = ka\sqrt{n^2 - n_{\text{air}}^2}$, where $k = 2\pi/\lambda$, $n = 1.452$ (SiO_2), $n_{\text{air}} = 1$; (i) fiber radius $a \simeq 300$ nm, (ii) $a = 215$ nm; single-mode ($V < 2.405$) shaded. **e,f,h)** Curves i-v: fiber radius $a = 215$ nm and toroid principal diameter $D_p = 12, 12.3, 12.6, 12.9, 13.2 \mu\text{m}$ (dashed red curves: $a = 300$ nm, $D_p = 12 \mu\text{m}$). **e)** t1, t2, t3: toroid whispering-gallery-mode with azimuthal mode numbers 117, 118, 119 respectively, $k_0 = 2\pi/\lambda$, $\lambda = 852$ nm. **f)** Transmittance T (x_{ft} is fiber-toroid gap). **g)** Oscillatory term P_{osc} of fiber-toroid coupling strength (fiber radius 215 nm (blue), 300 nm (red)). **h)** Transmittance T vs δL_{ft} , the deviation from L_{ft} value that maximizes P_{osc} , at critical coupling. 51
- 3.3 **Atom-toroid eigenenergy and spectrum.** **(a)** Imaginary part of the eigenvalues Λ_i of the linearized systems as a function of detuning $\Delta_{\text{ca}} = \omega_c - \omega_a$ for a Cs atom at $\phi = \pi/4$ and $g_{\text{tw}}/2\pi = 60$ MHz critically coupled to a cavity with parameters $\{\kappa_i, h\}/2\pi = \{8, 0\}$ MHz (Eqs. (3.15)). **(b)** Normalized transmission (red), T , and reflection (green), R , spectra as a function of cavity-atom detuning Δ_{ca} for $g_{\text{tw}} = 0$ and $g_{\text{tw}}/2\pi = 60$ MHz ($\theta = \pi/4$) at critical coupling. 56

- 3.4 **Microtoroid cavity QED experiment setup.** **a)** Schematic showing two ultra-high-vacuum chambers connected by a differential vacuum tube, where a magneto-optically trapped atom cloud is formed in the source chamber (left), loaded into an optical conveyor belt dipole trap formed by counter-propagating red-detuned beams λ_1, λ_2 whose relative frequency is chirped, transporting the atom cloud to the science chamber where a microtoroid and nanofiber is located, mounted on top of nanopositioners. **b)** CCD camera images of atom cloud fluorescence, showing source atom cloud (top left), cloud being transported to the toroid chip visible as a bright point (top right) and final position at $\sim 800 \mu\text{m}$ above the toroid chip (bottom panel). **c)** Top view. **d)** SEM images of a microtoroid and tapered fiber. **e)** Fresh (blank) optical table in 2007, showing parts to be used to build the setup from scratch. **f-h)** Completed setup where the experiments [10] and [5] were conducted, showing the main two-chamber setup in (f), various external cavity diode lasers, optical devices and optics supporting the experiment in (g), and Ti:Sapph laser (for optical conveyor belt) and home-built tapered amplifier units, with toroid characterization setup in the background (h). 62
- 3.5 **Tapered optical nanofiber.** **a)** Schematic of a tapered nanofiber, showing fiber jacket (diameter D_J), buffer (diameter D_B), tapering region (total end-to-end length L_T), nanofiber region (L_f) with uniform waist radius $a = D_f/2$, and fiber cladding (diameter D_{Cl}) and core (diameter D_{Cr}). Bottom: Two pair of blue- and red-detuned x -polarized beams form atom trapping potential as shown in b) and x -polarized probe beam shown by the gray arrow. **c)** Normalized electric field $|E|$ profiles and the components $\{E_x^\theta, E_y^\theta, E_z^\theta\}$ (where θ indicates the optical phase and location along the z -axis. E.g., $\theta = 0 \leftrightarrow z = 0, \theta = \pi/2 \leftrightarrow z = \lambda/4$) for the nanofiber fundamental HE_{11} mode polarized along x , with $E_x^{\text{max}} = 0.892|E|^{\text{max}}, E_y^{\text{max}} = 0.224|E|^{\text{max}}, E_z^{\text{max}} = 0.453|E|^{\text{max}}$. **d)** Theoretical prediction and experimental data of tapered fiber radius (r) profile along the fiber axis (z), measured from hundreds of SEM images taken from seven fabricated tapered fiber samples, such as the one shown in (iii). 72
- 3.6 **Electric field, $\mathbf{E}(x, y, z, t)$** of a single propagating beam in the plane $y = 0$. The input beam is x -polarized. The electric field $\text{Re}[\mathbf{E}(x, y, z, t)]$, with $\mathbf{E}(x, y, z, t)$ defined as in Eq. 3.27, is shown by the blue arrows. The red arrow indicates the beam propagation direction. The field is shown for **a)** $\omega t = 0$, **b)** $\omega t = \pi/2$, and **c)** $\omega t = \pi$ 74

- 3.7 **Total electric field, $\mathbf{E}(x, y, z, t)$** for two counter-propagating beams in the plane $y = 0$. The input beams are x -polarized. The electric field $\text{Re}[\mathbf{E}(x, y, z, t)]$ is shown by the blue arrows. The red arrows indicate the beams' propagation directions. The electric field is shown for **a)** $\omega t = 0$, **b)** $\omega t = \pi/4$, and **c)** $\omega t = \pi$. As opposed to Fig. 3.6, the polarization of the electric field is linear at any point $|\mathbf{r}| > a$ (i.e., the polarization vector has no ellipticity and \mathbf{E} does not rotate in time at a given position \mathbf{r} as in 3.6). 75
- 3.8 **Electric field amplitude after interference, $\mathbf{E}^{(\text{tot})} = \mathbf{E}^{(\text{fwd})} + \mathbf{E}^{(\text{bwd})}$** of two $\lambda = 937$ nm beams (x -polarized inputs with $\varphi_0 = 0$) with $\delta_{fb} = 0$, at $t = 0$ and $r = a_+$. The fields are normalized to the intensity I_0 at $r = a_+$, $\phi = 0$, $z = 0$. **a)** Axial direction z (at $\phi = 0$). **b)** Azimuthal direction ϕ (at $z = 0$). In particular, $\mathbf{E}^{(\text{tot})}$ has a fixed linear polarization at any given point \mathbf{r} which rotates as \mathbf{r} is varied. 76
- 3.9 **Nanofiber mode effective area.** Contour and cross-sectional plots of λ^2/A_{eff} showing atom-photon interaction strength profile, for a nanofiber HE_{11} mode, x -polarized in (a) and circularly-polarized in (b). The contour plot corresponds to nanofiber radius $a = 215$ nm. For the cross-sectional plots, the curves colored in red, blue, green, magenta correspond to $a = a_{\text{opt}} = 0.23\lambda = 196$ nm (the optimum fiber radius that holds for any λ ; here we choose $\lambda = 852$ nm), $a = 215$ nm, $a = 250$ nm, $a = 150$ nm respectively. . 77
- 3.10 **Tapered nanofiber fabrication and experiment overview.** **a)** Schematic showing a nanofiber mounted on an aluminium holder inside an UHV chamber, with three pairs of counter-propagating magneto-optical trapping and cooling beams forming cold atom cloud overlapped with the nanofiber. **b)** Photograph of the vacuum chamber, with arrow pointing towards the red-glowing nanofiber. **c, e)** Close-up and environment pictures of our old taper-pulling setup. **d, f)** Close-up and clean-hood environment pictures of our improved taper-pulling setup used to fabricate tapered nanofibers for our nanofiber atom trap experiment. 80

- 3.11 **Nanophotonic beam and mirror.** **a)** Schematic of a nanobeam device showing optical fiber to silicon nitride waveguide butt-coupling, adiabatic adapter to nanobeam mode (z_1 - z_6), a nanobeam waveguide with width w and height h , followed by a photonic crystal mirror (z_8 - z_9). The dimensions are discussed in the text. **b)** SEM images of a fabricated device (courtesy of Painter group), showing a sample structure with \sim mm size thru-hole in (i), fiber butt coupling (ii), nanobeam waveguide with electric field profile (iii), and photonic crystal mirror at the end (iv). **c)** Normalized electric field $|E|$ profiles and the components $\{E_x^\theta, E_y^\theta, E_z^\theta\}$ (where θ indicates the optical phase and location along the z -axis). E.g., $\theta = 0 \leftrightarrow z = 0, \theta = \pi/2 \leftrightarrow z = \lambda/4$ for the nanobeam fundamental HE_{11} mode polarized along x , with $E_x^{\text{max}} = 0.840|E|^{\text{max}}, E_y^{\text{max}} = 0.340|E|^{\text{max}}, E_z^{\text{max}} = 0.560|E|^{\text{max}}$ 83
- 3.12 **Single nanobeam mode effective area.** Contour and cross-sectional plots of λ^2/A_{eff} showing atom-photon interaction strength profile, for a single nanobeam fundamental x -polarized mode. **a)** The contour plot corresponds to nanobeam with width $w = 300$ nm and height $h = 200$ nm. **b)** For the cross-sectional plots, the curves colored in red, blue, green, magenta, brown, cyan, and orange correspond to single nanobeam with height $h = 200$ nm and width $w = 100, 150, 200, 250, 300, 350, 400$ respectively. Each row in (b) show the same curves, over a different domain. In the first column, the behavior close to the surface is more clearly shown while in the second column, the behavior far from the surface is more clearly displayed. 85

- 3.13 **Double nanophotonic beam and mirror.** **a, c)** Schematic of a double nanobeam device showing optical fiber to silicon nitride waveguide butt-coupling, adiabatic adapter to nanobeam mode, a Y-junction single-to-double beam mode converter, a double nanobeam waveguide with width w , height h , separated by a gap, followed by a photonic crystal mirror. The dimensions are discussed in the text. **b)** Dispersion curves showing effective refractive index $n_{\text{eff}} = \beta/k$ where $\beta =$ propagation constant of the guided mode, $k = 2\pi/\lambda =$ free-space wave number, $\alpha = 200$ nm and $n = 2.0$, of the first lowest order supermodes, for symmetric (even) modes: x -polarized (i) and y -polarized (ii), and anti-symmetric (odd) modes: x -polarized (iii) and y -polarized (iv). Higher-order modes start to appear beyond $V \simeq 3$ in the shaded region. **c)** Double nanobeam waveguide. **d)** Normalized electric field $|E|$ profiles and the components $\{E_x^\theta, E_y^\theta, E_z^\theta\}$ (where θ indicates the optical phase and location along the z -axis. E.g., $\theta = 0 \leftrightarrow z = 0, \theta = \pi/2 \leftrightarrow z = \lambda/4$) for the double nanobeam ($w = 300$ nm, $h = 200$ nm, gap = 200 nm) four lowest order modes polarized along x . For (i), $E_x^{\text{max}} = 0.920|E|^{\text{max}}, E_y^{\text{max}} = 0.440|E|^{\text{max}}, E_z^{\text{max}} = 0.429|E|^{\text{max}}$. For (ii), $E_x^{\text{max}} = 0.454|E|^{\text{max}}, E_y^{\text{max}} = 0.895|E|^{\text{max}}, E_z^{\text{max}} = 0.469|E|^{\text{max}}$. For (iii), $E_x^{\text{max}} = 0.863|E|^{\text{max}}, E_y^{\text{max}} = 0.445|E|^{\text{max}}, E_z^{\text{max}} = 0.572|E|^{\text{max}}$. For (iv), $E_x^{\text{max}} = 0.498|E|^{\text{max}}, E_y^{\text{max}} = 0.910|E|^{\text{max}}, E_z^{\text{max}} = 0.446|E|^{\text{max}}$ 87
- 3.14 **Double nanobeam mode effective area.** Plots of λ^2/A_{eff} showing atom-photon interaction strength profile, for a double nanobeam lowest-order x -polarized (even) mode. **a)** Contour plot corresponds to nanobeam with width $w = 300$ nm, height $h = 200$ nm and gap = 200 nm. **b)** Plot of λ^2/A_{eff} at $\{x, y\} = \{0, 0\}$ as a function of varying gap parameter. The curves colored in red, blue, green, magenta, orange correspond to double nanobeam with height $h = 200$ nm and width $w = 150, 200, 250, 300, 350$ nm respectively. **c-d)** Cross-sectional plots for double nanobeam structure with height $h = 200$ nm, varying widths w as labeled in each panel. For each panel, the gap size is scanned from gap = 100 nm (lightest blue) to gap = 500 nm (darkest blue) in steps of 50 nm. In c), the plots are along x -axis ($y = 0$), and in d), the plots are along y -axis ($x = 0$). 88

- 3.15 **Nanophotonic beams and cavities experiment setup.** **a)** Schematic of experimental setup showing two chambers separated by 70 cm connected by a differential pumping tube, where a magneto-optically trapped atom cloud is formed in the first chamber (i), pierced through by a near-resonant push beam (green arrow) that forms a jet of atoms, to be captured by a second magneto-optical trap in the science chamber (vi) formed by three pairs of counter-propagating beams shown by the red arrows, and in b). Following this stage, the cloud of atoms in the science chamber is transported and recaptured by a mini-magneto-optical trap inside the chip's thru-hole over the nanophotonic devices, formed by three pairs of small counter-propagating cooling and trapping beams shown in b). The setup is designed with multiple vacuum valves (ii), (iii), (iv) allowing frequent loading/unloading of nanophotonic device chip mounted on a multiplexer (vii) and translation stage (viii). **c)** Fluorescence image showing atom cloud transport from science chamber large MOT to mini-MOT inside the chip, taken with CCD camera with viewing direction shown by the cyan arrow in a) and b), also shown on the right panel of b). **d)** Setup built for our experiment. 90
- 4.1 **(a)** Simple depiction of one atom coupled to a toroidal cavity, together with fiber taper and relevant field modes, with rates $(g_{tw}, \kappa_{ex}, \kappa_i, h)$ as defined in the text. **(b-d)** Theoretical plots for the parameters of our experiment, $(g_{tw}, \kappa_{ex}, \kappa_i, h)/2\pi = (50, 300, 20, 10)$ MHz, with $\omega_A = \omega_C$. **(b, c)** Transmission and reflection spectra $T(\Delta), R(\Delta)$ for a_{out}, b_{out} as functions of probe detuning $\Delta = \omega_C - \omega_p$ with and without the atom. **(d)** Theoretical intensity correlation functions versus Δ for the transmitted $(g_T^{(2)}(\tau = 0))$ and reflected $(g_R^{(2)}(\tau = 0))$ fields. **(e)** Schematic of our experiment. 95
- 4.2 **(a,b)** Average atom transit signals for (a) transmission $\mathcal{T}_0(t)$ and (b) reflection $\mathcal{R}_0(t)$ of the probe field. As shown in the inset in (a), the transit selection criteria are set to be $C_{th} = 4, 5, 6$, where in all cases, $\Delta t_{atom} = 4\mu s$. **(c,d)** The intensity correlation functions $g_{T,R}^{(2)}(\tau)$ for the transmitted field a_{out} and the reflected field b_{out} . For (a-d), $\bar{n} = 0.093$ photons. Solid lines are a theoretical calculation using the parameters $(g_{tw}, \kappa_{ex}, \kappa_i, h)/2\pi = (50, 300, 20, 10)$ MHz. Dashed lines are the same calculation with 4% background counts. 99

- 4.3 **(a)** False detection ratio F , **(b)** transmitted signal $\mathcal{T}_0(t = 0)$ at the center of an atomic transit, and **(c,d)** intensity correlation functions $g_{T,R}^{(2)}(\tau = 0)$ at zero time delay for the transmitted T and reflected R light as functions of the threshold C_{th} for the selection of atom transits. In all cases, $\Delta t_{atom} = 4\mu s$ and $\bar{n} = 0.093$ 100
- 4.4 **(a)** Transmitted signal $\mathcal{T}_0(t = 0)$ at the center of an atomic transit and **(b)** intensity correlation function $g_R^{(2)}(\tau = 0)$ at zero time delay for the reflected light for various values of intracavity photon number \bar{n} . Points are experimental data averaged over individual transit events. Solid lines are from a theoretical calculation with the parameters $(g_{tw}^{min}, g_{tw}^{max}, \kappa_{ex}, \kappa_i, h)/2\pi = (35, 65, 300, 20, 10)$ MHz where instead of a single value of g_{tw} we use an average over g_{tw}^{min} to g_{tw}^{max} . Dashed lines are the same calculation, but with the assumption of background counts of 4% of the signal. 101
- 5.1 **Radiative interactions and optical potentials for an atom near the surface of a toroidal resonator.** **(a)** Simple overview of the experiment showing a cloud of cold cesium atoms released so that a few atoms fall within the evanescent field of a microtoroidal resonator. Light in a tapered optical fiber excites the resonator with input power P_{in} at frequency ω_p , leading to transmitted and reflected outputs P_T, P_R . **(b)** Cross section of the microtoroid at $\phi = 0$ showing the coherent coupling coefficient $|g(\vec{r}) = g(\rho, z, \phi)|$ for a TE polarized whispering-gallery mode. The microtoroid has principal and minor diameters $(D_p, D_m) = (24, 3) \mu m$, respectively. **(c)** (i) Coherent coupling $|g(d, z, \phi)|$ for the external evanescent field as a function of distance $d = \rho - D_p/2$ from the toroid's surface for $(z, \phi) = (0, 0)$. (ii) The effective dipole potentials U_d for resonant $\omega_p = \omega_a^{(0)}$, red $\omega_p < \omega_a^{(0)}$ and blue $\omega_p > \omega_a^{(0)}$ free-space detunings of the probe P_{in} (intracavity photon number ~ 0.1 , circulating power ~ 100 nW, circulating field intensity at surface $\sim 0.01 \mu W/\mu m^2$). The Casimir-Polder surface potential U_s for the ground state of atomic Cs is also shown. (iii) The atomic decay rate $\gamma(d)$ as a function of distance d from the toroid's surface for TE ($\gamma_{||}$) and TM (γ_{\perp}) modes. All rates in this figure are scaled to the decay rate in free space for the amplitude of the Cs $6P_{3/2} \rightarrow 6S_{1/2}$ transition, $\gamma_0/2\pi = 2.6$ MHz. The approximate distance scale probed in our experiment is $0 < d < 300$ nm. 106

5.2 **Observation (a) and simulation (b-e) of atomic transits within the evanescent field of the micro-toroidal resonator for $\Delta_{ca} = \Delta_{pa} = 0$.** **(a)** Observed cavity transmission $T_B(t)$ versus time t following a triggering event at $t = 0$, with approximately 5×10^4 triggered transits included. The data are fit to the sum of an exponential (I) and a Gaussian (II) (green curve), with time constants $\delta t_I = 0.78 \pm 0.02 \mu\text{s}$ and $\delta t_{II} = 3.75 \pm 0.09 \mu\text{s}$, with each component shown by the dotted lines. **(b)** Simulation result for 1000 triggered atoms for the cavity transmission $T_B^{(s)}(t)$ versus time t (points) from an ensemble of triggered trajectories. The green curve is a fit to the sum of an exponential and Gaussian with time constants $\delta t_I^{(s)} = 0.69 \mu\text{s}$, $\delta t_{II}^{(s)} = 4.0 \mu\text{s}$ while the dotted lines represent the individual fit components. **c-e** Probability densities $p_i(d), p_i(g), p_i(\delta_a)$ for the distance d , coupling g , and transition frequency shift $\delta_a = \omega_a(d) - \omega_a^{(0)}$ from the same simulation set as for (b). $\{d, g, \delta_a\}$ are averaged over the first 500 ns following the trigger. For these results, the trajectories are divided into two classes based on simulated detection events for photon transmission, $i = \{\text{I}, \text{II}\}$ corresponding to the two time constants $\delta t_I^{(s)}$ (blue shaded curve) and $\delta t_{II}^{(s)}$ (red shaded curve) in (b). This is a stochastic division and hence the distributions and trajectory characteristics show some overlap between sets I and II. Note: Intracavity photon number ~ 0.1 , circulating power $\sim 100 \text{ nW}$, circulating field intensity at surface $\sim 0.01 \mu\text{W}/\mu\text{m}^2$ 109

5.3 **Dynamics and trajectories for strongly coupled atoms moving in surface and dipole potentials $\{U_s, U_d\}$.** (a) Transmission $T(t)$ for $\Delta_{ca}/2\pi = -40$ MHz (left) and $+40$ MHz (right) measured after an atom trigger at $t = 0$. In each panel, the circles are data for 2×10^3 trigger events; the lines are simulations of $T(t)$ for the full model (blue), for $U_s = 0$ (magenta), and for $U_s = U_d = 0$ (green). Exponential fits to the data give time constants $\delta t_{\text{red}} = 0.11 \pm 0.01$ and $\delta t_{\text{blue}} = 0.53 \pm 0.03$ μs , while fits to the full simulation yield time constants $\delta t_{\text{red}}^{(s)} = 0.19 \pm 0.02$ μs and $\delta t_{\text{blue}}^{(s)} = 0.59 \pm 0.06$ μs , where quantitative differences are attributed to simplifications inherent in the simulation model (see SI). (b) Representative atomic trajectories projected onto the $\rho - z$ plane for simulations in panel (a), with the TE mode intensity plotted on a gray scale. The upper panels are for $\Delta_{ca}/2\pi = -40$ MHz while the lower panels are for $\Delta_{ca}/2\pi = +40$ MHz. The color bars at the top of the panels match the colors of the curves in (a). For each panel, orange lines are untriggered trajectories, while triggered trajectories are represented by blue lines which turn red after a trigger at $t = 0$. (c) Simulations showing trajectories from a full 3D simulation with U_s, U_d , as well as a two-color dipole potential (FORT) triggered “on” by atom detection at $t = 0$. $\Delta_{ca}/2\pi = +40$ MHz in correspondence to (a), (b). Blue lines represent falling atoms with the FORT beams “off” ($t < 0$), while red lines are trajectories after the FORT is triggered “on” and an atom begins to orbit the toroid. To illustrate the timescale, the trajectories are colored pink for $t > 50$ μs . Note: intracavity photon number ~ 0.1 , circulating power ~ 100 nW, circulating field intensity at surface ~ 0.01 $\mu\text{W}/\mu\text{m}^2$. . 111

- 5.4 **Transmission $T(\omega_p)$ and reflection $R(\omega_p)$ spectra for single atoms coupled to a microtoroidal resonator.** (a) cQED eigenvalues $\lambda_{\pm,0}$ for $\{h, g\}/2\pi = \{10, 40\}$ MHz as a function of atom-cavity detuning Δ_{ca} . The dashed lines indicate the detunings for the spectra in the following panels. (b) $T_i(\omega_p)$ for $\Delta_{ca}/2\pi = +60$ MHz for the empty cavity $i = \text{NA}$ (red) and with atoms $i = \text{A}$ (blue) calculated from a simple average for falling atoms over the distribution $p_{\text{fall}}(g)$ (inset) absent cavity and surface forces. $\Delta\omega_{\text{peaks}}$ is computed from the frequency difference for the peaks indicated by arrows. (c-d) Experimental reflection $R_i(\Delta_{pa})$ and transmission $T_i(\Delta_{pa})$ spectra with the peaks used for $\Delta\omega_{\text{exp}}$ indicated. Curves are results of the full Monte Carlo simulation and the color scheme is the same as in panel b. e Difference spectra $\Delta R = R_{\text{A}}(\Delta_{pa}) - R_{\text{NA}}(\Delta_{pa})$ and $\Delta T = T_{\text{A}}(\Delta_{pa}) - T_{\text{NA}}(\Delta_{pa})$ for $\Delta_{ca}/2\pi = +60$ (i,ii), $+40$ (iii,iv), -40 MHz (v,vi). Green lines are simulation results for $U_s = U_d = 0$, while blue lines are from the complete simulation. Error bars are estimated from photon counting statistics and systematic uncertainties. 113
- 5.5 **Photon statistics for localized atoms with $\Delta_{ca} = 0, \Delta_{pa} = 0$.** Cross-correlation $C_{12}(\tau)$ (blue circles) computed from the records of photoelectric counts at detectors D_1, D_2 from the forward flux P_T from a sum over many atom trajectories showing photon antibunching around $\tau = 0$, with $\bar{C}_{12}(\tau)$ obtained from the product of averages of the recorded counts at each detector for comparison (black circles). The red curve is a calculation for the two-time second-order correlation function from the full simulation scaled by a single parameter to match $C_{12}(\tau)$ at $\tau = \pm 40$ ns. (i) Expanded view of $C_{12}(\tau)$ and $\bar{C}_{12}(\tau)$ over full range of τ , with the long decay time of $\sim 2 \mu\text{s}$ originating from the atom transit times (Fig. 2a) and the classical variance between transits. . . . 116

- 5.6 **Schematic of microtoroidal cQED system.** (a) A microtoroidal resonator supports counter-propagating travelling wave modes $\{a, b\}$ coupled at a rate h . The circulating fields decay at a rate $\kappa = \kappa_i + \kappa_{\text{ex}}$ where κ_i is the resonator intrinsic loss rate and $\kappa_{\text{ex}} = \sqrt{\kappa_i^2 + h^2}$ is the coupling rate between the cavity and a tapered fiber at critical coupling. An optical switch controlled by an FPGA selects a driving field conditioned upon detection of an atom coupled to the cavity normal modes at a rate g . The all-in-fiber switch and beam splitter network delivers a power P_{in} to the microtoroid. Transmitted power P_{T} and reflected power P_{R} are detected by four single photon counting modules (SPCMs) and digitally recorded by a counter card. (b) A cloud of cesium atoms from a separate ‘MOT chamber’ is transferred via a differential pumping tube by an optical conveyor belt into the ‘science chamber’ and released 800 μm above a microtoroid. 117
- 5.7 **Real time detection of single atom transits.** (a) Normalized transmission spectra $T(\Delta_{\text{pa}})$ as a function of probe detuning Δ_{pa} for $g = 0$ and $g/2\pi = 50$ MHz ($\theta = 0$ and $\theta = \pi/4$) at critical coupling. The spectrum for $\theta = \pi/2$ is the mirror image of the $\theta = 0$ case about the $\Delta_{\text{pa}} = 0$ axis. (b) Transmitted photon flux as a function of g for $\Delta_{\text{pa}} = 0$. An atom trajectory with increasing g (say from $g = 0$ to $g/2\pi = 50$ MHz) results in increased P_{T} illustrated by the cyan arrow. (c) Experimental counts $C_1(t) + C_2(t)$ for 1501 transits from 596 atom drops with 4% false detection rate where the triggers are aligned at $t = 0$. (d) The same data aligned by redefining $t = 0$ to be the mean photon arrival time for each individual transit (blue). This alignment removes selection biasing seen in panel (a) and allows plotting of the distribution of trigger times relative to the transit center (red). Most triggers occur just prior to the peak of transmission of atom transits. The data in (c) and (d) have been smoothed for clarity, which artificially broadens the selection biasing effects in (c). In (b), (c) and (d) the maximum off-resonant transmitted photon flux is $P_{\text{T}} \approx 18$ MCts/s ~ 4 pW. 122
- 5.8 **Sample distributions $p(g)$ calculated for (a) $\Delta_{\text{ca}}/2\pi = 0$ and (b) $\Delta_{\text{ca}}/2\pi = +60$ MHz.** The analytic model is shown in red while the equivalent distribution from the Monte Carlo model with $U_{\text{d}} = U_{\text{s}} = 0$ is shown in blue. The distribution from the full Monte Carlo simulation with all potentials is shown in black for comparison. In both cases, the additional forces pull the distribution toward lower g 125

- 5.9 **Calculated atom-surface potential U_s^g for a Cesium atom at distance d from a SiO_2 surface with radius of curvature $R = D_m/2 = 1.5 \mu\text{m}$ (red) and $R \rightarrow \infty$ (blue).** The limiting cases for $R \rightarrow \infty$ are shown as dotted lines. In the region where surface forces are important, the cylindrical correction provides an accurate expression for the CP potentials. For $d > R$, the cylindrical correction formula is no longer valid. 127
- 5.10 **Experimental spectral data for various cavity detuning cases: (a) $\Delta_{ca}/2\pi = +40$ MHz. (b) $\Delta_{ca}/2\pi = -40$ MHz. (c) $\Delta_{ca}/2\pi = +60$ MHz.** In each difference spectrum, we plot the simulation for the full model (blue), $U_d = 0$ (cyan), and $U_s = 0$ (magenta), and $U_d = U_s = 0$ (green). The full simulation and $U_d = U_s = 0$ cases also appear in Fig.5.4. 128
- 6.1 **Variations of the dipole decay rate $\gamma_s(d)$ for a dipole oriented parallel (\parallel) and perpendicular (\perp) to the surface normal as a function of distance d from a semi-infinite region of SiO_2 .** The decay rate is in units of the vacuum decay rate γ_0 and the wavelength of the transition is $\lambda = 852$ nm. 137
- 6.2 **Dispersive response functions for SiO_2 and cesium atoms. (a)** The dielectric function $\epsilon(i\xi)$ for SiO_2 evaluated for frequency ξ along the imaginary axis. **(b)** Total atomic polarizability $\alpha(i\xi)$ evaluated for frequency ξ along the imaginary axis for the $6S_{1/2}$ ground state (red) and the $6P_{3/2}$ excited state (blue) of cesium calculated as described in 6.2.6. 138
- 6.3 **Atom-surface potentials U_s^g (red) and U_s^{ex} (blue) for a cesium atom at distance d from an SiO_2 surface.** The solid lines are for a planar surface whereas the dashed lines are for a curved surface with radius of curvature $R = D_m/2 = 1.5 \mu\text{m}$. The limiting regimes for U_s^g with a planar surface are shown as dotted lines, each calculated from analytic expressions not using the Lifshitz formalism. The cylindrical surface correction weakens the potential, which is noticeable in the retarded and thermal regimes. 140
- 6.4 **Plots of $T(g_{\text{tw}}, \theta, \mathcal{P})$ for (a) $\Delta_{ca}/2\pi = 0$ MHz, and (b) $\Delta_{ca}/2\pi = 60$ MHz, calculated numerically from (3.13).** Atoms with higher g_{tw} generally have higher T and a larger probability for detection. The variation of T with θ is evident, with a different periodicity for the two cavity detunings. 143

- 6.5 **Distributions $p_{t=0}(g)$ of coupling constants calculated for (a) $\Delta_{ca}/2\pi = 0$ and (b) $\Delta_{ca}/2\pi = +60$ MHz.** Distributions from the analytic model (red), semiclassical trajectory simulation with no dipole or surface forces (blue), and the simulation with all forces (black) are shown for comparison. (c) Experimental cQED spectra data for cavity detuning $\Delta_{ca}/2\pi = 60$ MHz (blue points) from [5] plotted with model spectra calculated from the distributions $p_{t=0}(g)$ in panel (b). The red is the analytic model of Section 6.2.7 and black is the semiclassical simulation. 144
- 6.6 **Probability distribution $p_{t=0}(\theta)$ of atomic azimuthal angle $\theta = m\phi \bmod 2\pi$ at transit detection time $t = 0$ presented as histograms of simulation runs.** Shown are the cases for cavity detunings (a) $\Delta_{ca} = 0$ (green) and (b) $\Delta_{ca}/2\pi = +40$ MHz (blue) and $\Delta_{ca}/2\pi = -40$ MHz (red, semi-transparent). Normalization is such that the sum across all θ is unity. 145
- 6.7 **Simulated trajectories for model parameters $\mathcal{P}_{1,2}$ ($\Delta_{ca}/2\pi = 40$ MHz) plotted for four models of radiative forces: the full semiclassical model, $U_s = 0$, $U_d = 0$, and $U_s = U_d = 0$.** For the full model, a three-dimensional representation is shown, while trajectories are projected onto the two-dimensional $\rho - z$ plane for all conditions. Magenta trajectories represent *un-triggered* atoms, blue paths are detected atoms for $t < 0$ and red paths represent atom trajectories after the trigger for $t > 0$. . . 147
- 6.8 **(a)** The trapping potential U_t along the $z = 0$ axis with the CP potential included. Also shown are the red and blue evanescent potentials of the two trapping modes, U_t , respectively. **(b)** The mode function used in U_t for the 898 nm mode with $m = 106$. **(c)** Simulated trajectories for trapping simulations with an eFORT U_t triggered “on” by atom detection at $t = 0$ with $\Delta_{ca} = 0$. Falling atoms with the FORT beams “off” ($t < 0$) are colored blue, whereas trajectories after the trap is triggered are red. Trajectories are colored pink for $t > 50 \mu\text{s}$ to illustrate the timescale. Roughly 25% of the triggered trajectories become trapped. **(d)** Same as (c) showing only the trapped trajectories and a clearer view of atom orbits in the evanescent trap. Note: this figure appears in [228]. 155

- 6.9 **Whispering gallery modes of a microtoroid.** **a)** Transverse cross-sectional plots showing electric field amplitude $|E|$ for the first six modes of a silica microtoroid with principal diameter $D_p = 24 \mu\text{m}$ and minor diameter $D_m = 3 \mu\text{m}$, for z -polarized (unprimed labels) and ρ -polarized (primed labels) modes. **b)** Plots of azimuthal mode number m as a function of toroid's resonance frequencies f , showing a 'forest' of modes in the spectrum, for $m = 117$ (red), $m = 118$ (blue), and $m = 119$ (green). The plots in a) corresponds to $m = 118$. **c)** Sensitivity of resonant frequency for $m = 118$, z -polarized mode (the mode used in the experiment described in Chapter 5) as a function of principal diameter D_p (for minor diameter $D_m = 3 \mu\text{m}$) and temperature change δT in Kelvin. 158
- 6.10 **Nanofiber atom trap and microtoroid cavity scheme.** **a)** Top view of experimental setup for atom trapping next to a microtoroidal cavity using a tapered nanofiber. Right diagram: Atom cloud transported by a free-space optical conveyor belt (one-dimensional dipole trap lattice) formed by counter-propagating red-detuned beams (red arrows), which is loaded into a nanofiber trap (formed by two pairs of red- and blue-detuned beams using our magic-compensated scheme described in Chapter 7, red and blue arrows) as it is cooled by polarization-gradient cooling beams (green arrows), and transported along the fiber by another optical conveyor belt to the toroid. The gold mirror provides reflections of the cooling beams (green arrows) in the vertical plane, and the copper plate provides thermal conductivity for cavity temperature control. **b)** Photon counts measured at the output of the fiber coming from fluorescence of atom cloud in the conveyor belt trap at the science chamber (overlaped with tapered fiber). The y -axis is the ratio of photon counts with atom and without atom, $C_{\text{atom}}/C_{\text{noatom}}$. A resonant pumping beam that illuminates the atom cloud and nanofiber in the cooling beam direction labeled (i) is turned on at $t = 0.04 \text{ ms}$, and turned off at $t = 0.9 \text{ ms}$. . . 161

- 6.11 **Trapping atoms near a nanofiber and a microtoroid.** **a)** Schematic of a microtoroidal cavity and a nanofiber for trapping atoms in the evanescent field of the toroid's whispering gallery mode. **b)** Dipole trap potential U around the nanofiber far away from the toroid, using the fundamental HE_{11} mode of the nanofiber (radius $a = 215$ nm) is shown by curve (i) in a) and b). The left end of the plot is at $x = x1 = 215$ nm (the fiber's surface), while $x = x6$ is the toroid's surface for the trap potential curve (ii) in b) and a), which takes into account the even and odd supermodes as equal superpositions. The almost vertical line at $x = x2$ represents the Casimir-Polder potential 'cliff' that diverges to $-\infty$ at the nanofiber surface. **c)** Electric field amplitude $|E|$ profiles for the lowest order even and odd supermodes for $\lambda = 687$ nm and 937 nm, treating the nanofiber and toroid as two silica parallel cylindrical waveguides with diameters 430 nm and $3 \mu\text{m}$ respectively. **d)** Trap potentials, U , at the closest approach plane (ii) in a), for $F=4$ ground state (thick colored curves), $F=3$ ground states (black dashed curves), and $F'=4$ excited states (thin colored curves). The same set of red curves are shown in b) and d). The orange curve in d) shows the atom-toroid coupling rate g , with $g/2\pi = 20, 30, 45$ MHz at $x3, x4, x5$ respectively. A typical experimental value for the total cavity decay rate achieved for the toroid geometry considered as described in Chapter 5 is $\kappa/2\pi = 20$ MHz. 165
- 7.1 **Nanofiber atom trap scheme.** **a)** Schematic of our magic-compensated nanofiber trap scheme, consisting of two pairs of red- and blue-detuned counter-propagating x -polarized beams. **b)** Electric field profiles for x -polarized $\lambda_{\text{red}} = 937$ nm red-detuned (first row) and $\lambda_{\text{blue}} = 687$ nm blue-detuned (second row) beams on the $x - y$ plane (second column) and $x - z$ plane (third column), with 3D cartoon illustration in first column. **c)** Other schemes utilizing pair of red-detuned beams and a single blue-detuned beam, with orthogonal and parallel polarizations in (i) and (ii) respectively. **d)** Ground state (cesium $6S_{1/2}, F = 4$) trap potential for the scheme shown in a) with $\lambda_{\text{red}} = 937$ nm, $P_{\text{red}} = 2 \times 0.4$ mW, $\lambda_{\text{blue}} = 687$ nm, $P_{\text{blue}} = 2 \times 5$ mW, nanofiber radius $a = 215$ nm, with a simple Casimir-Polder potential $U_{\text{CP}} \sim -1/r^3$ near the surface of nanofiber. 170

7.2 **Effectiveness of the magic-compensated trapping scheme.** **a)** (i) Nanofiber trap scheme of [248] (orange color code); (ii) Our magic-compensated trap scheme (cyan color code), with magic wavelengths for the $6S_{1/2}, F = 4 \rightarrow 6P_{3/2}, F' = 4$ transition of the Cs D_2 line shown in (iii) and (iv). The light shifts U_{ls} are for a linearly polarized beam with constant intensity $2.9 \times 10^9 \text{ W m}^{-2}$ around (iii) the blue-detuned magic wavelength at $\lambda_{\text{blue}} \simeq 684.9 \text{ nm}$ and (iv) red-detuned magic wavelength at $\lambda_{\text{red}} \simeq 935.3 \text{ nm}$. **b)** Atom energy levels for the configuration shown in (i) of a), orange color code, using parameters of [248]. Trap minimum is located at $r_{\text{trap}} - a = 230 \text{ nm}$ from the fiber surface, where the fiber radius is $a = 250 \text{ nm}$. **c)** Atom energy levels for the magic-compensated scheme shown in (ii) of a), cyan color code, using the parameters $\lambda_{\text{red}} = 935.3 \text{ nm}$, $P_{\text{red}} = 2 \times 0.95 \text{ mW}$ and $\lambda_{\text{blue}} = 684.9 \text{ nm}$, $P_{\text{blue}} = 2 \times 16 \text{ mW}$. Trap minimum is located at $r_{\text{trap}} - a = 200 \text{ nm}$ from the fiber surface, where the fiber radius is $a = 250 \text{ nm}$. **b-c)** The energy sublevels of the ground states $F = 3$ and $F = 4$ of $6S_{1/2}$ are shown as solid green and dashed black curves, and the $F' = 4$ sublevels of the electronically excited state ($6P_{3/2}$) are shown as red dashed curves. In the first column are radial trap potentials ($\phi = z = 0$); second column, axial trap potentials ($r = r_{\text{trap}}, \phi = 0$); and third column, azimuthal trap potentials ($r = r_{\text{trap}}, z = 0$). In c), the compensation configuration leads to suppression of energy level splitting spreads due to vector shifts of the blue-detuned beams, and the use of magic wavelengths minimizes differential energy shifts between the ground and excited states. 178

7.3 Trapping potential for nanofiber atom trap experiment with magic-compensated

scheme. a-b) Adiabatic trapping potential U_{trap} for a state-insensitive, compensated nanofiber trap for the $6S_{1/2}, F = 4$ states in atomic Cs outside of a cylindrical waveguide of radius $a = 215$ nm. Contour plots show U_{trap} for the ground state $F = 4$ of $6S_{1/2}$. For the cross-sectional plots, U_{trap} for the substates of the ground level $F = 4$ of $6S_{1/2}$ (excited level $F' = 5$ of $6P_{3/2}$) are shown as black (red-dashed) curves. **(a)(i)** azimuthal $U_{\text{trap}}(\phi)$, **(ii)** axial $U_{\text{trap}}(z)$ and **(b)** radial $U_{\text{trap}}(r - a)$ trapping potentials. The trap minimum for $6S_{1/2}$ is located at about 215 nm from the fiber surface. Input polarizations for the trapping beams are denoted by the red and blue arrows in the inset in (b). Here we utilize a pair of counter-propagating x -polarized ($\varphi_0 = 0$) red-detuned beams ($P_{\text{red}} = 2 \times 0.4$ mW) at $\lambda_{\text{red}} = 937.1$ nm, and counter-propagating, x -polarized blue-detuned beams ($P_{\text{blue}} = 2 \times 5$ mW) at $\lambda_{\text{blue}} = 686.1$ nm as described in Sec. 7.4. The resulting interference is averaged out by detuning the beams to $\delta_{fb} = 382$ GHz. Due to the complex polarizations of the trapping fields, the energy levels are not the eigenstates of the angular momentum operators, but rather superposition states of the Zeeman sublevels. Note that there were errors in our initial calculation in [142], which led to the magic wavelength values $\lambda_{\text{red}} = 937.1$ nm and $\lambda_{\text{blue}} = 686.1$ nm, used in our experiment. The correct magic wavelength values are $\lambda_{\text{red}} = 935.3$ nm and $\lambda_{\text{blue}} = 684.9$ nm [64]. The plots in this figure are based on the corrected equations [64], for the actual wavelengths used in our experiment, $\lambda_{\text{red}} = 937.1$ nm and $\lambda_{\text{blue}} = 686.1$ nm. 182

7.4 Tapered optical nanofiber fabrication. **a)** Schematic of tapered fiber pulling setup. (1a-c): Motorized and manual stages for $\text{H}_2\text{-O}_2$ torch mount. (2a-c): Hydrogen-oxygen torch, with a 1.2 mm diameter single-orifice nozzle as shown in part c) (iii) of figure. (3a-b): Computer controlled, high precision motorized linear stages. (3c): Custom aluminium adapter blocks. (3d): Magnetic fiber clamps. (4b): Bare fiber to be tapered. **b-c)** Photographs of setup and components. (5a): Precision manual translation stage used to hold experiment aluminium taper holder during gluing process. (4a): Photodetector monitoring optical power transmission of fiber during pulling. (6a-b): Microscope imaging and illumination. (10a-b): $\text{H}_2\text{-O}_2$ gas mass flow controllers and filters. (7a): Air current shield used in pulling process. (8a): Class-100 cleanhood. (9a): Flexible stainless steel braided gas hoses. (4a): Thermal fiber stripper. 186

- 7.5 **Taper pulling motorized stages position and velocity trajectories. a-g)** Position and velocity trajectories programmed to the heating (i)-(ii) and pulling (iii)-(iv) motors shown in h). **a)** Heating stage position, z_h , as a function of time t , with the first 10 seconds of the sequence shown in b). **c)** Heating stage velocity, v_h , as a function of time t , also shown in d) for the first 10 seconds. **e, g)** Pulling stage position (z_p) and velocity (v_p) trajectories. The insets in a) and c) show expanded views of the plots. In (a,c,e,g), the time t_1 corresponds to the optimized end time of the trajectory sequence run used in our nanofiber fabrication, where in the time $t = 0 \rightarrow t = t_1$, z_h moves by z_{h1} in the negative direction, and z_p moves by z_{p1} in the positive direction (see part h)). To avoid abrupt motion at the turning points, the heating stage changes direction in velocity with a sinusoidal profile over 100 ms as shown in (i) in d), expanded in f). The computer controller takes all of the position and velocity trajectory inputs and moves the motorized stages with high precision and smooth trajectories up to the jerk (time derivative of acceleration). **h)** The motion of the stages from the start ($t = 0$) to end ($t = t_1$) pulled the fiber (v) heated by the flame (vi) from length L_0 to length L_1 . 189
- 7.6 **Tapered nanofiber shape. a)** Theoretical prediction (curves) and measurement data points of seven fabricated tapered nanofiber samples, showing the taper radius (r) as a function of position (z) along the fiber axis. The shaded region between (i) and (iii) shows the taper radius range where it is most critical to have a small slope ($\frac{dr}{dz}$) to ensure adiabaticity and high taper transmission efficiency. **b)** The plot in logarithmic scale, showing the exponential decay profile (linear in logarithmic scale) and uniform waist radius at the 6 mm center nanofiber region. **c)** Expanded view around the nanofiber waist, showing theoretical curves for heating length $L_w = 6$ mm (i) and $L_w = 5.9$ mm (ii), and data points where circled data points are averaged and shown as the sample waist radii in d). **e)** Data points and theory curve for one of the seven samples. **f)** Hundreds of SEM images from seven samples like these make up the data points in a-e). 192

7.7 **Adiabaticity condition and nanofiber transmission efficiency.** **a)** Cross-sectional plot showing taper radius (r) along the fiber axis (z) and the local slope $\theta(z) = \arctan(\frac{dr}{dz})$. **b)** Histogram of $N = 57$ total fabricated taper samples, with number of samples $N = 41$ for $T \geq 90\%$, and $N = 26$ for $T \geq 95\%$. **c)** Normalized guided mode propagation constant β/k , $k = 2\pi/\lambda$, $\lambda = 852$ nm as a function of taper radius (r), for core-cladding modes, HE_{11} (1a, blue) and HE_{12} (1b, black), and cladding-air modes, HE_{11} (2a, red) and HE_{12} (2b, green). The expanded plot for these HE_{11} (2a, red) and HE_{12} (2b, green) modes are shown in d). The dashed line (ii) in c) and e) show the radius where β (for HE_{11} core-cladding mode) is closest to β (for HE_{12} cladding-air mode), where it is most critical to suppress the slope $\frac{dr}{dz}$, to avoid excitation of the higher-order mode HE_{12} that would lead to transmission loss as it will leak out at the small radius region where it is not supported by the waveguide ($r < 0.5 \mu\text{m}$ as can be seen in panel d)). The shaded region bounded by (i) and (iii) represents the region close to this critical radius (ii). **e)** Simulation of fiber profile slope $\frac{dr}{dz}$ as a function of z ; (top) adiabaticity criterion (black) with $\pm 3\%$ taper radius (green) and $\pm 10\%$ taper radius (red); (bottom) stochastic simulation of the slope distribution of 100 taper pulling runs, using motorized stages with higher specification (orange) vs lower specification (blue). **f)** Stochastic simulation of 100 taper pulling runs result showing $\pm 2\%$ nanofiber waist radius spread for the higher spec stages (i) and $\pm 5\%$ radius spread for the lower spec motorized stages (ii). Details of the motorized stages specifications are discussed in the text. 193

- 7.8 **Scatterers and contamination on nanofiber samples.** **a)** Faint glow visible from a nanofiber in a clean and good condition. **b)** Brighter glow as cleanliness decreases, but the glowing from Rayleigh scattering is still uniformly distributed, suggesting absence of large scatterers. **c)** One large scatterer can be observed, associated with the bright glowing point. One large scatterer such as this could be sufficient to induce local heating and melting with optical guided power of 10-100 μW inside vacuum environment. The setup in the photo here is in air (not in vacuum). **d)** Numerous large scatterers observed. The photos in a-d) were taken over a period of about 30-40 minutes with ≈ 10 minutes interval. **e)** Plastic shielded area below a HEPA-filtered cleanhood fans above our experiment setup. Here clean air current could keep a nanofiber sample inside the space clean for multiple days. **f-j)** SEM images of broken (melted by guided optical power) tapered nanofiber which had been exposed to cesium atoms inside a vacuum chamber. 197
- 7.9 **Nanofiber atom trap setup.** Schematic of the setup for a state-insensitive, compensated nanofiber trap. VBG: volume Bragg grating, DM: Dichroic mirror, PBS: polarizing beamsplitter, and APD: avalanche photodetector. The inset shows an SEM image of the nanofiber for atom trapping. 198

- 8.1 **Single nanobeam waveguide single atom transmittance and reflectance with atom-surface induced level shifts.** **a)** (i) Atom ground state Casimir-Polder level shift as a function of atom-to-surface distance d . Solid curves: $U_g = A \times C'_3/d^3$, where C'_3 is the van der Waals coefficient for cesium and silicon nitride (infinite planar) surface, and $A = 1, 1/2, 1/3, 1/4$ for the black, red, green, blue curves respectively. The black data points are a full simulation taking into account the finite nanobeam's closest surface height (height $h = 200$ nm, infinite length), calculated using finite element method by Chen-Lung Hung [110]. (ii-iii) Atom's transition frequency shift δf due to differential level shift of the ground and excited state ($U_e = 2U_g$). **b-c)** Transmittance (T) and reflectance (R) of a single nanobeam waveguide with a single atom located at atom-to-surface distance along the x -axis (i.e., at $y = 0$), dx , for a single nanobeam with height $h = 200$ nm, and width $w = 100, 150, 200, 250, 300, 350, 400$ nm corresponding to the red, blue, green, magenta, brown, cyan, orange curves respectively. Part c) shows the same curves as part b) but across different range to highlight the longer distance behavior. **d-e)** Transmittance (T) and reflectance (R) of single nanobeam waveguide with a single atom located at atom-to-surface distance along the y -axis (i.e., at $x = 0$), dy , for a single nanobeam with height $h = 200$ nm, and width $w = 100, 150, 200, 250, 300, 350, 400$ nm corresponding to the red, blue, green, magenta, brown, cyan, orange curves respectively. 206

8.2 **Cold atom cloud near a single nanobeam structure.** **a)** Schematic of a silicon chip with a $3 \text{ mm} \times 1.5 \text{ mm}$ through-hole with five nanophotonic devices butt-coupled to five optical fibers, and a cold atom cloud overlapping the center device, shown in (i). Part (ii) shows a close look of the center single nanobeam photonic device with butt-coupler at one end, a photonic crystal mirror at the other end, and a cold atom cloud centered on the uniform nanobeam waveguide section at the center. Part (iii) shows a schematic of the single nanobeam waveguide, showing the nanobeam's width w , height h , and the coordinate system $\{x, y, z\}$. Part (iv) shows the fundamental x -polarized mode normalized electric field amplitude $|E|$ for a single nanobeam of width $w = 300 \text{ nm}$ and height $h = 200 \text{ nm}$. The mode area in this $x - y$ cross-sectional plane is approximated by the rectangle of width x_0 and height y_0 as illustrated. An atom nearby this silicon nitride nanobeam has an initial velocity v associated with the thermal cloud velocity distribution for a given temperature T_{cloud} , several forces acting on the atom including gravity (F_g), surface force (F_s), and optical forces (F_{opt}) from the magneto-optical trapping and cooling beams. **b)** Number of atoms (N_{atoms}) that are on average in the vicinity of a single nanobeam's evanescent field region as a function of atom cloud density (ρ), located within a volume of $V = V_0 = 2 \times x_0 \times y_0 \times L$, where $x_0 = 100 \text{ nm}$, $y_0 = 100 \text{ nm}$, and $L = 500 \mu\text{m}$ for the red curve (labeled (ii)). The curves labeled (i) and (iii) in blue and green correspond to twice ($V = 2V_0$) and half ($V = 0.5V_0$) volumes respectively. **c)** Transit time ($\Delta t_{\text{transit}}$) of an atom with an initial rms velocity v directed downwards, which is accelerating in gravity, not taking into account surface (F_s) nor optical (F_{opt}) forces. The curves labeled (i), (ii), (iii) in blue, red, green correspond to an atom falling down over a distance $y_0 = 200, 100, 50 \text{ nm}$ respectively, where $\Delta t_{\text{transit}}$ is the time the atom takes over the distance y_0 208

- 8.3 **Cavity QED with a single nanobeam and cavity frequency temperature tuning.** **a-b)** Cooperativity parameter C as a function of the atom-to-surface distance along the x -axis ($y = 0$), dx , for a cesium atom (D2 transition, $\lambda = 852$ nm), for a single nanobeam x -polarized mode, with cavity length $L_{\text{cav}} = 500$ μm and finesse $\mathcal{F} = 100$ (giving cavity FSR = 149 GHz (or 0.36 nm), quality factor $Q = 2 \times 10^5$, and cavity decay rate $\kappa/2\pi = 4.67$ GHz), with nanobeam height $h = 200$ nm, and width $w = 100, 150, 200, 300, 400$ nm for the green, magenta, black, red, blue curves respectively. **c-d)** Tuning curves of wavelength and cavity resonance frequency as a function of wavelength λ , based on thermo-optic ($\frac{dn}{dT}$), thermal expansion ($\frac{dL}{dT}$) coefficients for silicon nitride, $\frac{dn}{dT} = 10^{-5}$ K^{-1} , $\frac{dL}{dT} = 0$ and 3.2×10^{-6} K^{-1} for the blue and red curves respectively. **e)** Atom-photon coupling rate g . **f)** Critical atom and photon numbers, N_{ca} and N_{cp} . **g-h)** Atom-photon coupling rate g as a function of the y coordinate, at $dx = 0$ in g) and at $dx = 100$ nm in h). In parts e-h), the blue (and cyan) curves correspond to a cavity length $L_{\text{cav}} = 500$ μm and finesse $\mathcal{F} = 1000$, the red (and magenta) curves $L_{\text{cav}} = 250$ μm and finesse $\mathcal{F} = 1000$, and the black curves $L_{\text{cav}} = 250$ μm and finesse $\mathcal{F} = 2000$. The horizontal lines show the corresponding (color-coded) total cavity decay rates κ . Note that the single nanobeam is symmetrically centered at the origin ($x = y = 0$) in the $x - y$ cross-section, with its axis going out-of-page along the z -axis, as illustrated in Fig. 3.11. Note: Here we do not include Casimir-Polder effects. 212

8.4 **Experimental setup. a-b)** A magneto-optically trapped (MOT) cloud of atoms is formed in the source chamber (a), pushed by near-resonant beam towards the science chamber (e) through a weak differential pumping tube (b), bellow and fittings (c-d), over a distance $L1 \approx 70$ cm. The source and science chambers have background pressures of $\sim 10^{-9}$ torr and $\sim 10^{-10}$ torr respectively. Chamber (e) is continuously kept at ultra-high vacuum by the ion pump (f), located at $L2 \approx 70$ cm. Atoms transported from the source chamber are collected at the science chamber by a second MOT with three orthogonal large (≈ 2 cm diameter) retroreflected beams. **c)** After a compression stage, the atom cloud (i) is transported (ii-iii) into the through-hole of the chip where the device is (iv) by moving the quadrupole magnetic field zero from (i) to (iv). The atoms are then collected by a third MOT, a mini-MOT, formed by three orthogonal small (≈ 1 mm diameter) retroreflected beams intersecting at the center of the chip's through-hole. Here, about $\sim 10^6$ atoms are collected (density $\sim 10^{10}$ atoms/cm³). **d)** Fluorescence image showing the second MOT in chamber (e). **e)** Absorption images showing atom cloud transport starting from the second MOT location (i), during transport (ii-iii), and the mini-MOT location inside the chip's through-hole (iv). . . . 216

8.5 **Atom trapping schemes with a single nanobeam (part 1).** **a-b)** Trapping potential U for magic-compensated scheme (similar to Sec. 7.2). a) and b) show the same curves over different plot ranges. Single nanobeam width $w = 400$ nm, height $h = 200$ nm (Fig. 3.11). Red-detuned standing-wave ($\lambda_{\text{red}} = 937.1$ nm, power $P_{\text{red}} = 2 \times 0.4$ mW) and counter-propagating blue-detuned beams ($\lambda_{\text{blue}} = 686.1$ nm and 686.7 nm). dy: atom-to-surface gap along y -axis ($x=0$). Blue, red, magenta, green curves for $P_{\text{blue}} = 2 \times \{1, 2, 3, 10\}$ mW respectively. Thin curves: excited state ($6P_{3/2}$, $F=4$), thick curves: ground state ($6S_{1/2}$, $F=4$), black-dashed curves: ground state ($6S_{1/2}$, $F=3$). Orange curve (iv): normalized atom-photon coupling rate g , for a cavity length $L_{\text{cav}} = 1$ mm, finesse $\mathcal{F} = 1000$, FSR = 74 GHz (or 0.18 nm), $Q \approx 5 \times 10^6$, and cavity decay rate $\kappa/2\pi = 234$ MHz. At the surface ($dy=0$, $x = 0$), $g/2\pi = 1.15$ GHz. Dotted lines (i), (ii), and (iii) correspond to distances ($dy = 138$ nm, 260 nm, 392 nm) where $g = 4 \times \kappa$, $2 \times \kappa$, and κ respectively. **c-d)** Trapping scheme using orthogonal polarizations. **c)** Decay lengths L_x and L_y of the electric field amplitude $|E|$, $|E| = |E|_0 \exp(-dx/L_x)$ (similarly for L_y), where $|E|_0 = |E|$ at the surface. dx: atom-to-surface gap along x -axis ($y = 0$), dy: along y -axis ($x = 0$). x -polarized mode (red, magenta): (i) and (ii) for L_x and L_y respectively; y -polarized mode (blue, cyan): (iii) and (iv) for L_x and L_y respectively. Here, nanobeam height $h = 200$ nm, width w . **d)** Trap potential U for a red-detuned y -polarized standing wave ($\Delta\nu_{\text{red}} = -350$ GHz, power $P_{\text{red}} = 2 \times 6 \mu\text{W}$) and a blue-detuned x -polarized traveling wave ($\Delta\nu_{\text{blue}} = +350$ GHz, power $P_{\text{blue}} = 200 \mu\text{W}$) for a nanobeam width $w = 360$ nm, height $h = 200$ nm, trapping along the y -axis. **e-f)** External illumination trap scheme. Plots show electric field amplitude $|E|$ of a $300 \text{ nm} \times 200 \text{ nm}$ silicon nitride beam above a $700 \text{ nm} \times 200 \text{ nm}$ silicon beam with vertical surface-to-surface gap of 450 nm, where a single red-detuned ($\lambda_{\text{red}} = 937$ nm) plane-wave illumination light beam polarized in the z -axis (out of page) is propagating downwards. 222

- 8.6 **Atom trapping schemes with a single nanobeam (part 2).** Normal incident incoherent counter-propagating red-detuned external illumination light trapping scheme. The single silicon nitride nanobeam has a width of $w = 300$ nm and height $h = 200$ nm. The external counter-propagating illumination beams have a wavelength $\lambda_{\text{red}} = 852.55$ nm with a small \approx GHz relative detuning, and total intensity $I_{\text{red}} = 2 \times 32 \mu\text{W}/\mu\text{m}^2$ (i.e., total power of $P_{\text{red}} = 2 \times 10$ mW for a beam waist radius $\approx 10 \mu\text{m}$). **a)** Contour plot of trap potential U as a function of the x -coordinate and atom-to-surface distance along the y -axis ($x = 0$), dy. **b)** Line cut along the y -axis ($x = 0$) showing the trapping potential. The red curves correspond to cesium excited state ($6P_{3/2}$, $F'=4$), the blue curves correspond to the ground state ($6S_{1/2}$, $F=4$), and the black-dashed curves that correspond to the ground state ($6S_{1/2}$, $F=3$). **c-d)** Contour plots of electric field amplitude $|E|$ on the $x-y$ cross-sectional plane, where the nanobeam's waveguide axis is along the z -axis (out of page). The white arrows indicate the external illumination beams. **e-f)** Line cuts of $|E|$ of the corresponding contour plots, along the y -axis ($x = 0$) shown by the blue curves (i), and along the x -axis ($y = 0$) shown by the red curves (ii). 226

- 8.7 **Atom trapping schemes with a single nanobeam (part 3).** **a-b)** Counter-propagating coherent red-detuned beams (black arrows) forms a standing wave pattern. Single nanobeam has a width of $w = 300$ nm, height $h = 200$ nm, and the illumination light has a wavelength $\lambda \approx 852$ nm. Here the two light beams are phase-locked relative to each other, and relative to the SiN nanobeam. The phase-locked standing wave is shifted vertically along y -axis by 200 nm for plot b) relative to plot a). **c-f)** Hybrid external side illumination and guided mode trapping scheme, with same SiN nanobeam dimensions. A red-detuned side illumination beam has a wavelength of $\lambda_{\text{red}} = 852.55$ nm, a power of $P_{\text{red}} = 1$ mW for a beam cross-sectional radius of $10 \mu\text{m}$, shining towards the $+x$ direction, with electric field polarized in the z -axis (out-of-page); and a blue-detuned counter-propagating x -polarized guided mode beam (wavelength $\lambda_{\text{blue}} = 852.15$ nm, power $P_{\text{blue}} = 2 \times 0.5 \mu\text{W}$). **c)** Trap potential U as a function of y coordinate and atom-to-surface distance along x -axis, dx . **d)** 3D plots illustrating the trapping potential U as a function of dx and y in (i), and in (ii), for a tilted side illumination Poynting vector, at 10° angle from the x -axis, on the $x - y$ plane. **e-f)** Line cuts of U from c), which is the same as in d) (i). Red curves: excited state ($6P_{3/2}$, $F'=4$), blue curves: ground state ($6S_{1/2}$, $F=4$), black-dashed curves: ground state ($6S_{1/2}$, $F=3$). 229

- 8.8 **Atom trapping schemes with a double nanobeam (part 1).** **a-b)** Coherent side illumination with an auxiliary beam. Here we consider two red-detuned beams ($\lambda_{\text{red}} = 937$ nm, polarized along the z -axis, out of page) shining from the $-x$ and $+x$ directions, tilted by $\theta = 15^\circ$ from the horizontal axis as shown by the white arrows. Double beam parameters: (each beam: width $w = 300$ nm, height $h = 200$ nm) separated by a gap of 400 nm along the x -direction. The auxiliary SiN nanobeam (width 400 nm, height 200 nm) is 600 nm below the double nanobeam (surface-to-surface). **c-h)** Corrugated double SiN nanobeam trapping scheme. Cross-sectional contour plots for a propagating wavelength around 852 nm, calculated in 3D with periodic boundary condition. Total periodic cell length, $d1 = 1$ μm , thickness, $d2 = 200$ nm, width of the larger beam, $d3 = 200$ nm, width of the center beam, $d4 = 100$ nm, length of the center beam, $d6 = 500$ nm (centered along the periodic structure axis, i.e., along $d1$, z -axis), and the surface-to-surface inner gap between the larger beams, $d5 = 600$ nm. The coordinate system $\{x, y, z\}$ is shown in d). **c,e,g)** show a y -polarized mode, where we see a local intensity minimum in three-dimensions as shown in the $y-z$, $x-y$, $x-z$ cross-sectional planes in c), e), g) respectively. **d,f,h)** show an x -polarized mode, where here we see a local intensity maximum in three-dimensions as shown in the $y-z$, $x-y$, $x-z$ cross-sectional planes in d), f), h) respectively. 231

8.9 **Atom trapping schemes with a double nanobeam (part 2).** Scheme utilizes red- and blue-traps in guided modes. Double SiN nanobeam parameters: each beam: width $w = 300$ nm, height $h = 200$ nm, gap between the two along x direction is 200 nm. **a-g)** Trap potential U formed by a counter-propagating red-detuned x -polarized beams (wavelength $\lambda_{\text{red}} = 853$ nm, power $P_{\text{red}} = 2 \times 10 \mu\text{W}$) providing axial (z -axis, out-of-page) confinement; and a single (traveling wave) y -polarized blue-detuned beam (wavelength $\lambda_{\text{blue}} = 851$ nm, power $P_{\text{blue}} = 4$ mW) for transverse confinement. Casimir-Polder potential: $U = -C_3/d^3$ with $C_3^g = 1972 \text{ Hz } \mu\text{m}^3$ and $C_3^{\text{ex}} = 2899 \text{ Hz } \mu\text{m}^3$, for two ($y - z$) SiN planes located at $x = -100$ nm and $x = 100$ nm. **a,b)** Potential U in the $x - y$ and $x - z$ planes. **d,f)** Line cuts along z -axis ($x = y = 0$) and x -axis ($y = z = 0$) respectively. Horizontal lines in f): $U = 0$. Red curves: excited state ($6P_{3/2}$, $F'=4$), blue curves: ground state ($6S_{1/2}$, $F=4$), black-dashed curves: ground state ($6S_{1/2}$, $F=3$) in d-g). Part c) shows the ground state ($6S_{1/2}$, $F=4$) potential U line cuts along x -axis ($y = z = 0$) and y -axis ($x = z = 0$) with curves colored in red and blue respectively. **e)** Potential U for the radius $r = 25$ nm (where $r = 0$ at the origin, located at $x = y = 0$, the center of the gap between the two SiN nanobeams), as a function of the azimuthal angle ϕ in the $x - y$ plane (where $\phi = 0$ for $x > 0, y = 0$, $\phi = 45^\circ$ along the line $y = x$ for positive x and y , and $\phi = 90^\circ$ for $y > 0, x = 0$). The inhomogeneous broadening due to the vector shifts are largest at $\phi = 45^\circ$. **g)** Close-up version of part e) for ϕ between 43° and 47° . **h)** Inhomogeneous broadening spread ΔU for $\phi = 45^\circ$ as a function of radius r 234

8.10 **Atom trapping schemes with a double nanobeam (part 3).** Two-color RF switching scheme. Double Si nanobeam parameters: (each: width $w = 300$ nm, height $h = 200$ nm), gap along the x -axis is 200 nm. Switching between red- and blue-detuning for an x -polarized even mode forms a pseudo trap potential analogous to a quadrupole Paul trap in ion trap systems. **a)** Illustration of sinusoidal oscillation between maximum blue-detuned beam intensity at time t_{blue} , (i), with a trap along x -axis and an anti-trap along y -axis, transition time through t_{both} , (ii) to (iv), to maximum red-detuned beam intensity (zero blue-detuned beam intensity) at time t_{red} , (v), followed by the reverse cycle (arrows). In part a), the effective potential δU corresponds to the trapping potential using the parameters described below, with offset applied to the potential U , i.e., $\delta U = U(x, y) - U(x = y = 0)$, such that $\delta U(x = y = 0) = 0$ at all time. The time-dependent offset $U(x = y = 0)$ ranges from -0.86 mK (at time t_{red} , (v) in a)) to +6.25 mK (at time t_{blue} , (i) in a)). On the $x - y$ plane, the origin ($x = y = 0$) is at the symmetry center between the two double beam. **b,d)** Trap potential U formed by a standing wave blue-detuned beam (wavelength $\lambda_{\text{blue}} = 851$ nm, power $P_{\text{blue}} = 2 \times 20 \mu\text{W}$). **d)** Red curve (i): line cut along x -axis ($y = 0$). Blue curve (ii): line cut along y -axis ($x = 0$). **c,e)** Trap potential U formed by a standing wave red-detuned beam (wavelength $\lambda_{\text{blue}} = 853$ nm, power $P_{\text{blue}} = 2 \times 1 \mu\text{W}$). **e)** Red curve (i): line cut along x -axis ($y = 0$). Blue curve (ii): line cut along y -axis ($x = 0$). 238

A.1 **(a)** x-Attocube. **(b)** z-Attocube. **(c)** Attocube piezo scan controller ANC200 for fine motion (top) and piezo step controller ANC150 for coarse motion (bottom). 239

A.2 **(a)** Schematic of setup. **(b)** z-Attocube (stacked) setup. **(c)** x-Attocube (single) setup. Shown in (b) and (c) are: mirror (A), aluminium block (B) and block (C). 240

A.3 **Calibration factor** (piezo displacement per applied voltage) distributions for a single x-Attocube for 0.5 Hz and 5 Hz sweep frequencies. 241

A.4 **Attocube transfer functions** highlighting intrinsic mechanical resonances associated with the four configurations: (a)/(b) Single/stacked x-Attocube; (c)/(d) Single/stacked z-Attocube. 242

List of Tables

1.1	Descriptions and numerical values used for Figure 1.1. The relevant time scale for comparison, Δt , is 1 second in most cases except for certain processes as listed.	3
8.1	Thermo-optic (dn/dT) and thermal expansion (dL/dT) coefficients for silicon dioxide (SiO_2) and silicon nitride (SiN). As the effective wavelength λ increases as temperature increases, the effective optical frequency f decreases.	213
A.1	Summary of load masses, interferometer fringe visibilities, and triangular wave sweeping amplitudes for Attocube calibration for the four configurations.	240
A.2	Summary of calibration factor results for triangular wave sweeps at 0.5 Hz and 5 Hz. Sample size refers to the number of calibration factors computed. Range is calculated based on 0-150 V voltage range for 5 Hz sweep values.	241
A.3	Summary of Attocube intrinsic mechanical resonances.	242